Dynamic numerical modelling of co-seismic landslides using the 3D distinct element method: insights from the Balta rockslide (Romania)

Anne-Sophie Mreyen[a,*], Davide Donati[b], Davide Elmo[c], Frederic Victor Donze[d] and Hans-Balder Havenith[e]

[a]Urban & Environmental Engineering, University of Liege, 4000 Liège, Belgium
[b]Department of Civil, Chemical, Environmental, and Materials Engineering, Università di Bologna, 40126 Bologna, Italy
[c]Norman B. Keevil Institue of Mining Engineering, University of British Columbia, Vancouver, BC V6T 1Z4, Canada
[d]ISTerre, Université Grenoble Alpes, 38400 Saint-Martin-d'Hères, France
[e]Department of Geology, University of Liege, 4000 Liège, Belgium

ARTICLE INFO

Keywords:
flysch rockslide
geomodelling
slope reconstruction
internal fracturing
numerical modelling
back-analysis

ABSTRACT

Ancient landslides of unknown origin can be found in large numbers in hilly and mountainous regions; some represent valid markers of (pre-)historic natural regimes referring to either long-term evolution or short-term peak events of climatic and seismotectonic nature. The Balta rockslide in the Romanian Carpathian Mountains represents such a key site: its location in the seismically active Vrancea-Buzau region, as well as its morphological features, deep-seated shape and large debris volume, raise the question of its failure history with regard to a possible co-seismic triggering. A 3D volume based reconstruction of the slope morphology together with field measurements of elasto-plastic in-situ rock properties allow to estimate pre-failure conditions of the slope, with special regards to the geological, i.e. flysch bedrock of poor to fair rock quality, and structural, i.e. anti-dip slope bedding crossed by the main joint family, settings of the slope. The reconstructed slope behaviour was tested under static and dynamic forces with the 3D distinct element code 3DEC (Itasca), subsequently used to simulate a failure scenario with a 120 s long real earthquake record that leads to the actual post-failure morphology of Balta. For the latter, we observe a principally joint-guided failure combined with internal fracturing of the intact rock mass. After 230 s of simulated time, the landslide debris reaches the valley bottom with maximum displacements of 1350 m and is marked by a lateral expansion to a broader extent than the source zone width, as observed in the field. Extended analyses of this work to other pre-historic slope failures in the valleys of Vrancea-Buzau can constitute valuable new information for future seismic hazard estimations of the region.

1. Introduction

The characteristics, scale and effects of co-seismic landslides depend on multiple aspects that are linked to the energy of the associated seismic event and to the local settings of the affected rock slope (Keefer, 1984; Khazai and Sitar, 2004; Sassa, 1996; Romeo, 2000). Such factors comprise the shaking intensity of the seismic event, which depends on the epicentral distance, focal mechanism and depth, and the energy transmission to the slope, which is affected by the local geological, structural and morphological setting.

Various site-specific factors are known to intensify the seismic impact on slopes: (1) topographic effects, depending on the slope morphology in terms of steepness, height and curvature, can result in amplification of incident seismic

*Corresponding author
as.mreyen@uliege.be (A. Mreyen)
ORCID(s): 0000-0003-3449-9754 (A. Mreyen)

waves (especially at slope and mountain crests; cf., Havenith et al., 2003b; Sepúlveda et al., 2005; Meunier et al., 2008; Huang et al., 2012; Maufroy et al., 2015); (2) geological and structural effects, comprising lithological predispositions (e.g., high impedance contrast between geological formations; cf., Bozzano et al., 2008; Bourdeau and Havenith, 2008; Luo et al., 2019) as well as structural settings (e.g., sliding prone dip angle and orientation of bedding planes or discontinuities, possibly coupled with reduced joint strength; cf., Willenberg et al., 2008; Stead and Wolter, 2015; Scholtès and Donzé, 2015); (3) weakened surface material, conditioned by micro- to macro-scale fracturing, weathering or long-term fatigue (cf., Moore et al., 2011; Gischig et al., 2015; Burjánek et al., 2018); (4) hydrogeological regime changes as a result of intense precipitation events and fluctuating groundwater pressures as well as seismic-induced effects such as liquefaction (cf., Iverson et al., 1997; Wang and Sassa, 2003, 2009).

Engineering geology models, established with numerical modelling codes, are a common tool to analyse the effects of seismic waves on a rock slope (e.g., Bozzano et al., 2008; Pal et al., 2012; Gischig et al., 2015, 2016; Song et al., 2020; Luo et al., 2020; He et al., 2020). Numerical simulations are largely applied in the analysis of anisotropic and jointed rock slopes (e.g., Kim et al., 2015; Bonilla-Sierra et al., 2015; Che et al., 2016; Li et al., 2019), taking into account the discontinuity of rock mass as an important factor for the overall slope stability, as they can be crucial for seismic wave propagation as well as amplification and polarization effects.

For (pre-)historic seismic landslides, the comprehension of interacting factors that are at the origin of the slope failure can be quite challenging. However, as outlined by Crozier (1992) and Jibson (1996), the study of paleoseismic landslides allows to better understand the paleoseismicity of a region, provided they can be dated and their co-seismic origin can be shown. In general, the failure history of ancient landslides in seismic regions is difficult to infer and extensive understanding of past interactions between seismic loads, geological-geomechanical conditions and local site effects is required. Various studies back-analyse the development of (pre-)historic rock slope failures with a possible seismic history using numerical modelling techniques, such as Singeisen et al. (2020) for the 3.2 ka old Kandersteg rock avalanche, Swiss Alps, Bozzano et al. (2011) for the historic Scilla rock avalanche triggered by the 1783 Calabria earthquake, South Italy, or Zhu et al. (2019) for the seismically triggered Tahman paleolandslide in the eastern Pamir, Northwest China.

In this paper, we study a paleo-rockslide in the flysch belt of the Carpathian Mountains of Romania, located in the seismic region of Vrancea-Buzau (see Figure 1), which presents morphological features that suggest a co-seismic origin (see description of study site in section 2 about the landslide's source area, depth and volume). Furthermore, this site allows for an experimental approach of slope reconstruction to pre-failure conditions, and for testing factors in the static and dynamic domains that possibly led to the present-day slope shape. In regard to the seismic context of the region, we are particularly interested in the effects of dynamic simulations of the slope - in a broader perspective, the latter can help to identify slopes such as Balta as marker of the pre-historic seismic activity of the Vrancea-Buzau region in Romania. In earlier works, Lemaire et al. (2020) studied the structural setting of the Balta slope, while Mreyen et al. (2021) analysed its geomorphic features and characterized the slide deposits as well as the in-situ sedimentary rock with geophysical methods. Here, we estimate a pre-failure state of the rock slope, i.e. prior to landsliding, and test the impact of seismic loading in realistic conditions with numerical modelling using 3DEC (3-dimensional distinct element code, version 5.2; Itasca, 2016).

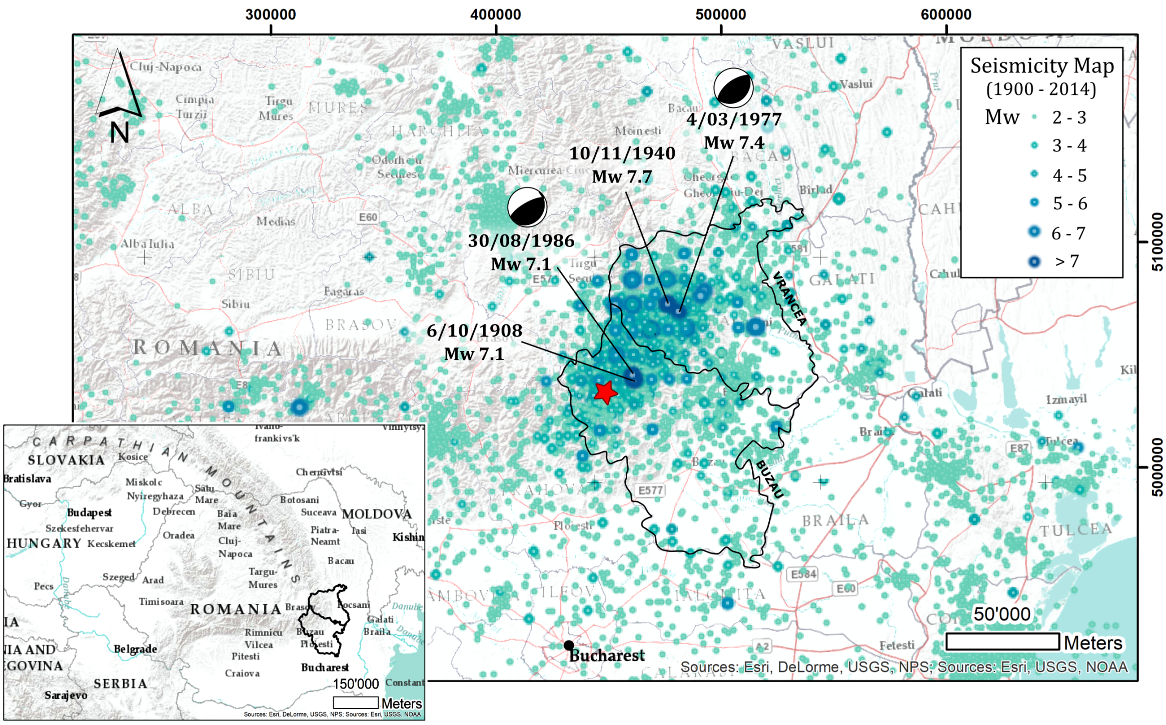

Figure 1: Location of the study area (marked by red star) in the seismic region of Vrancea-Buzau, Romania, after Mreyen et al. (2021).

2. Study site

The ancient Balta rockslide can be classified as rock rotational slide (after the classification of Hungr et al., 2014), presenting distinct morphologies such as a detachment scarp of approximately 250 m height (visible from the valley) and a large plateau area generated by the landslide deposit (Figure 2a and 2c). The studies of Mreyen et al. (2021) established a maximum depth of the landslide rupture surface at 70-90 m depth using a combination of active and passive seimic methods, and inferred a landslide volume of approximately 28.5-33.5 million m³. The geophysical measurements highlighted the intense fracturing and fragmentation of the material constituting the landslide body, particularly within foot and toe, while more massive sandstone blocks can be found near the source area. In general, the flysch rock properties of the study area can be described as weak (estimated GSI of 35-45 after Marinos et al., 2000); weaker elastic properties were measured at the nearer slope surface (< 50 m) (Mreyen et al., 2021). The slide developed in a Paleogene schistose sandstone flysch formation that is dominated by thick sandstone banks, apparent along the outcropping rupture zone (Figure 2d) and presenting an anti-dip slope bedding (i.e. geological layers dip into the slope - in contrast to a dip slope, where layers dip into the valley). The work of Lemaire et al. (2020) analysed the structural setting of the source rock, i.e. 40-50° inclined bedding planes towards S-SE with a strike of N48°E (marked in red in Figure 2e), and crossing discontinuities, i.e. two joint families, the first predominated by a Fisher mean plane of 56/331 and a secondary, with 74/223 (marked in green and blue in Figure 2e, respectively).

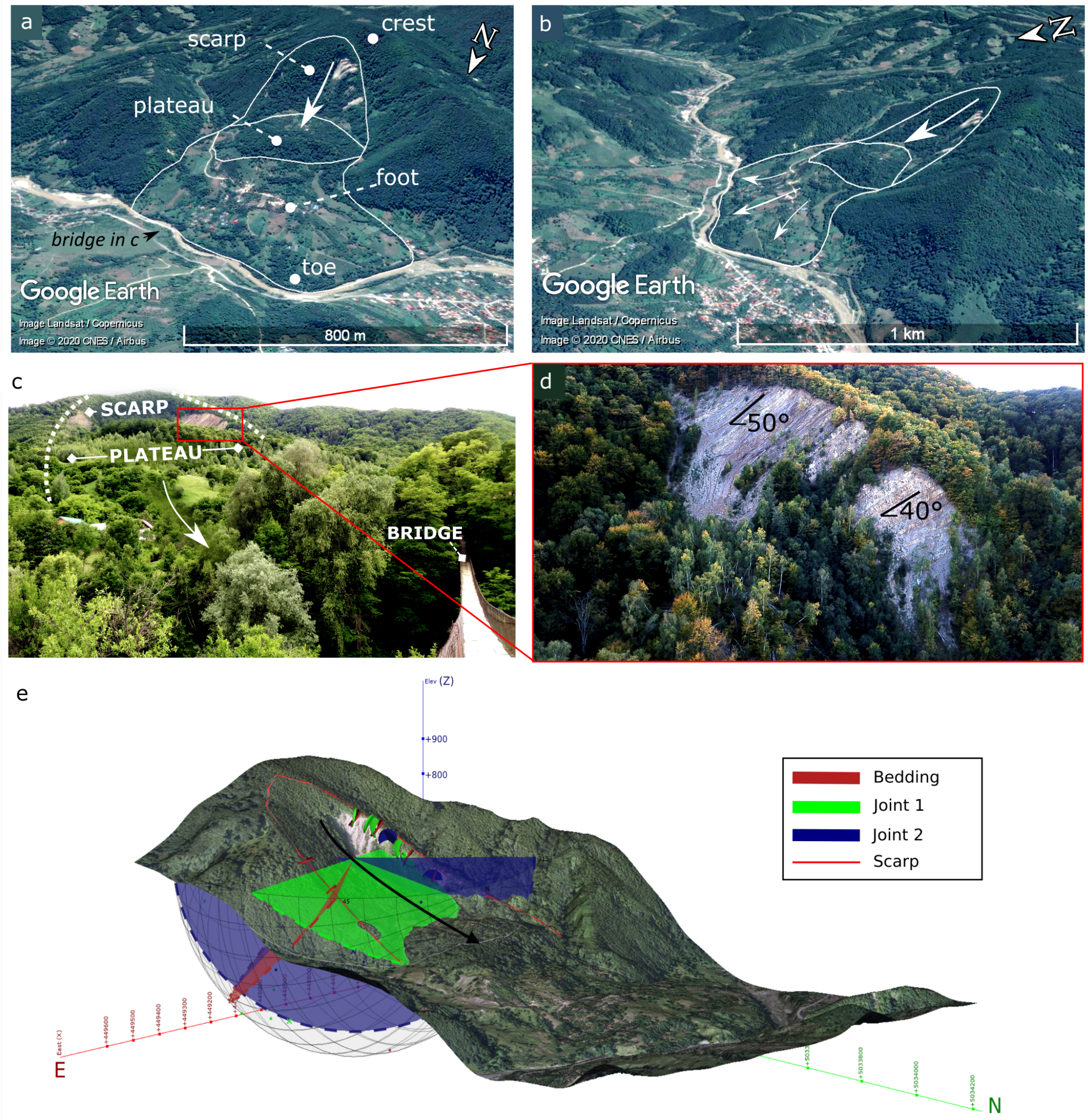

Figure 2: Google Earth© imagery of the Balta rockslide: (a) geomorphic overview; (b) expansion and spread of landslide material marked by white arrows. Structural setting of the Balta rockslide: (c) photo taken from the valley in June 2017; (d) UAV image of the outcropping flysch bedding at the scarp after Mreyen et al. (2021); (e) structural model showing the flysch anti-dip slope bedding and crossing joint families after Lemaire et al. (2020).

Flysch can be classified as highly anisotropic sedimentary rock, composed of alternating layers of hard (limestone, sandstone or siltstone) and weaker (claystone, mudstone or marl) materials, which increases the complexity for geotechnical parametrisation (cf., Marinos and Hoek, 2001). Stability analyses of flysch slopes have been presented by several authors, e.g., Baron et al. (2005); Berti et al. (2017); Kogut et al. (2018); Krawiec and Harba (2019), testing rock strength and joint conditions in 2D. In general, numerical analyses of natural slopes have been largely presented in the two-dimensional domain; however, three-dimensional analyses of natural slope behaviour are rather scarce, especially in a seismic context. An example for the latter are recent studies of Luo et al. (2020), who analyse amplification effects over a natural slope affected by seismic shaking in the visco-elastic domain with the 3D distinct element method.

The necessity of a three-dimensional back-analysis of the Balta slope is given by its post-failure geometry that is marked by the rather narrow, but steep and profound, detachment scarp, while the relatively large volume of landslide sediments fans out into the valley (towards N), predominated by a lateral expansion (E-W orientated; cf., Figure 2b). The movement is thus presumed to be a three-dimensional problem, that due to the nature of debris distribution cannot be solved along a single section. To account for the particular morphological, geological and structural setting in conjunction with the seismic context of the study area, the presented analysis tests both static and dynamic forces.

3. Methodology

3.1. Slope reconstruction

Based on the volume estimation of debris mass accumulated in the study area, an estimation of the Balta morphology prior to failure was realised using the established geomodel of the slope (Fig. 3a; cf. Mreyen et al., 2021). Various studies attempt reconstructions of pre-event morphologies, such as Singeisen et al. (2020) who used contour lines and point cloud interpolations in GIS software. Here, the slope reconstruction was performed using multiple 2D cross sections as input for surface mesh construction, and thus accounting for the final 3D volume balance of the slope by respecting a mass bulking factor of 15%, i.e. volume gain due to failure, computed similar to recommendations by Hungr and Evans (2004); Jaboyedoff et al. (2019). The used 3D volume balancing (difference of elevation models, cf., Zangerl et al., 2015) stands in contrast to the standard 2D volume balance cross section method using one single cross section for a respective site ('section area balance', cf., Zangerl et al., 2015). The reason for the application of the 3D volume balance method is the central source zone of the failure together with the lateral expansion of the landslide mass at the foot of the slope, i.e. mass motion is not exclusively downwards. In this case, a 3D reconstruction allows best to establish a correct volume balance between the pre- and post-failure state of the slope (here, computed with the Leapfrog Geo software, Seequent, 2021). Figure 3 shows three examples of the 2D cross sections, where the actual landslide mass is coloured in green, and the dotted line outlines the reconstructed topography. The section shown in Figure 3a.1 marks the most pronounced central crest established in the reconstruction, whereas the defined slope angle diminishes towards West as shown in Figure 3a.2. For sections crossing the lateral expansion of the landslide mass, the reconstructed topography results in a negative mass balance, i.e. the pre-failure slope estimates less mass to be in place than in its actual state (Figure 3a.3). In total, 25 sections were used to create slope reconstruction curves; these latter were interpolated to a 25 m-resolution mesh, using the radial basis function (RBF) implemented in the Leapfrog software, that constitutes the modelled pre-failure topography. The reconstructed pre-failure topography displays a central N-S orientated ridge along which a maximum slope angle of 54° is noted. A secondary ridge, oriented NE-SW, is implemented parallel to alignments of neighbouring mountain ridges (analysed using LiDAR digital elevation models of the studied region). The landslide foot area was levelled to 400 m a.s.l, implying that the river valley was located south to the actual water course before slope failure. Figure 3b displays the final reconstructed slope model that is used as input geometry for the numerical analysis described in the following section.

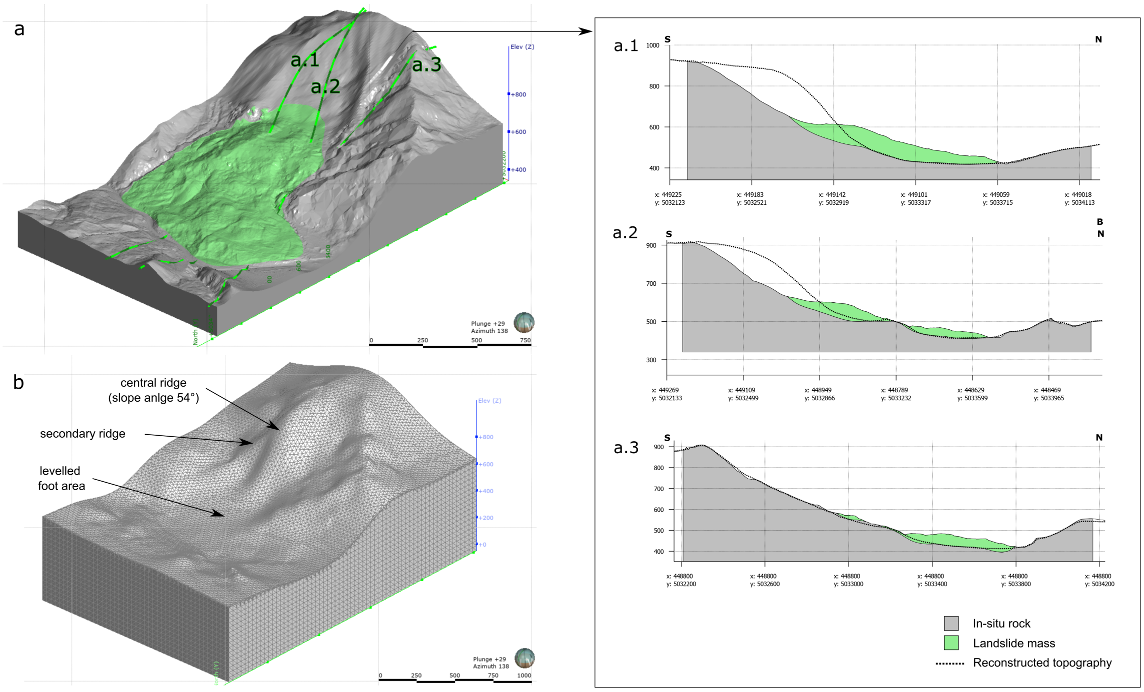

Figure 3: Slope reconstruction of the Balta landslide: (a) actual, i.e. post-failure (presented in Mreyen et al., 2021), morphology with landslide mass marked in green - the three cross sections (a.1-3) show exemplary 2D reconstruction cruves; (b) reconstructed, i.e. pre-failure, morphology with surface mesh resolution of 25 m.

3.2. Distinct element modelling

3.2.1. Model setup

In a first step, the created pre-failure surface mesh was processed with the CAD software Rhino 5.0 (McNeel et al., 2010) and the Itasca plug-in Griddle 1.0 (Itasca, 2019). In Rhino, the lateral and basal surface boundaries of the 3D model were created and merged with the pre-failure morphology to create a closed 3D block model; another surface, that is later used to distinguish the weaker near-surface material (cf., description of the study site and Mreyen et al., 2021), was modelled by duplicating the topographic mesh 50 m below its origin. Further structural elements, notably the rock bedding planes (cf. model composition shown in Figure 6b), were also implemented in the CAD software to facilitate element discretization. An unstructured surface and volume mesher were applied to the model domain, creating tetrahedral elements with edge lengths of 30 to 90 m, while the smallest elements are located close to the model surface to optimally emulate the topography. The created source area model was imported into 3DEC 5.2 (Itasca, 2016); it covers a surface of 1646 m width and 2400 m length and spans a vertical range of -50 to 992.4 m a.s.l. (see Figure 4) with the model bottom fixed at a sufficiently large depth in order to guarantee full wave length transmission from bottom to top for the dynamic slope analysis. The model orientation is defined by the x-axis in E-W direction, y-axis in N-S direction and the vertical z-axis. Distinct elements were made deformable by creating uniform finite-difference (FD) tetrahedral zones of 30 m edge length within the polyhedron blocks (fixed according to Eq. 7).

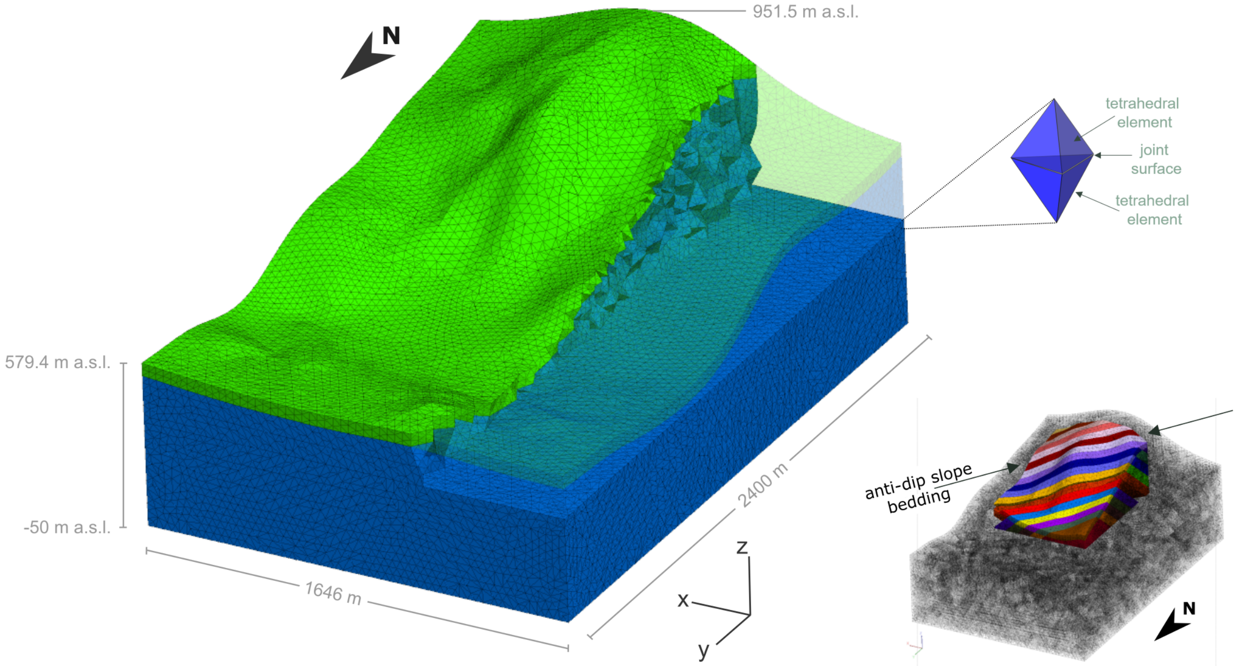

Figure 4: Model setup of the Balta slope in 3DEC; green and blue differentiate the near-surface and intact bedrock material, respectively. The inset figure in the lower right illustrates the modelled anti-dip slope layering of the flysch bedrock.

The model domain was defined for elasto-plastic Mohr-Coulomb (M-C) material behaviours of rock mass, while the discontinuities were Coulomb-slip enabled. Table 1 lists the physical properties used for the rock block material; the elastic rock parameters were defined on the basis of the geophysical surveys performed in the study area, presented in Mreyen et al. (2021). Due to the lack of laboratory tests (given the challenge of extracting a rock sample adequate

Table 1
Elastic and Mohr-Coulomb (M-C) material parameters of the rock mass for the near-surface and the intact bedrock.

Rock mass		Near-surface	Intact bedrock
Elastic	Density ρ $[kg/m^3]$	2000	2400
	Young's modulus E $[GPa]$	1.7	10.7
	Bulk modulus K $[GPa]$	2.1	9.6
	Shear modulus G $[GPa]$	0.6	4.1
	Poisson's ratio ν $[-]$	0.37	0.31
	P-wave velocity V_P $[m/s]$	1200	2500
	S-wave velocity V_S $[m/s]$	550	1300
M-C	Cohesion C $[MPa]$	0.01	1
	Tension σ_T $[MPa]$	0.005	0.5
	Internal friction angle ϕ [°]	42	45

Table 2
Strength properties of the discontinuities for the near-surface and the intact bedrock.

Discontinuities		Near-surface	Intact bedrock
Coulomb slip	Joint normal stiffness Jk_N $[GPa]$	0.1	1
	Joint shear stiffness Jk_S $[GPa]$	0.05	0.5
	Cohesion c $[kPa]$	5	10
	Residual cohesion c_r $[kPa]$	0	0
	Tensile strength T $[kPa]$	0.1	1
	Residual tensile strength T_r $[kPa]$	0	0
	Friction angle φ [°]	40	42
	Residual friction angle φ_r [°]	28	30

for geotechnical laboratory testing) and the scale discrepancy between laboratory and field conditions, the plastic rock mass parameters were indirectly derived using average rock properties for similar lithotypes (mi=15, UCS=75 MPa) provided in the RocLab software database (Rocscience, 2002), and considering a GSI of 35-45 (based on field estimates). Due to the rather weak and highly strained in-situ flysch bedrock and as observed for the landslide debris mass in the field, we aim to simulate fracturing of "intact" bedrock material, an approach that is revised by Donati et al. (2018) and applied, e.g., in the study of Gischig et al. (2015) simulating rock fatigue after repeated seismic stresses of a 2D slope using Voronoi tessellation. In our case, this approach allows to reproduce internal fracturing of the landslide material that takes into account the behaviour of the flysch rock mass itself next to the structural aspects of the slope. The strength properties of the discontinuities, thus representing the defined joint structures as well as boundary conditions between blocks, are listed in Table 2 (note, the interfaces between tetrahedrals were assigned the same properties as the discontinuity sets to account for the intense structural damage that characterize the rock mass). The values assigned to the 50 m thick near-surface layer (see green layer in Figure 4) account for the poor material and joint strength due to weathering effects and possibly tectonic fatigue, as observed by geophysical tests on in-situ rock in the study area (cf. Mreyen et al., 2021). Residual values are assigned by the system as soon as initial slip has occurred.

The kinematic behaviour of blocks during numeric cycling is monitored using seven history points at surface and three history points inside the model, set to log displacement, velocity, and acceleration in the x (i.e. East-West), y (i.e. North-South), and z directions (see Figure 5).

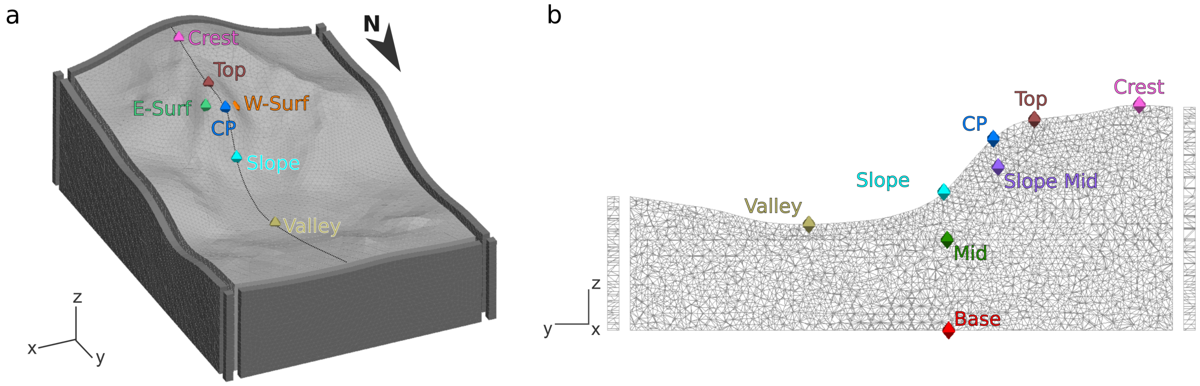

Figure 5: Position of history points at the model surface (a) and within the model (b); position of cross section is marked by the projected line in (a).

In total, six different internal model structures were tested during the numerical analysis of Balta as illustrated in Figure 6 along a 2D cross section of the slope. The complexity of model structure was increased progressively during the modelling process as they depend on computational capacities. The basic structure consists of the slope material (intact bedrock) and the near-surface material presenting weaker material strength (Figure 6a). The other structures (Figure 6b-d) intend to analyse, separately and jointly, the effect of bedding planes and joint sets in the slope. Dip angles and orientations of discontinuities were assigned in accordance to the field measurements (presented in Lemaire et al., 2020).

3.2.2. Static conditions

The static modelling domain seeks a (non-inertial) model solution of static force-equilibrium under gravitational forces as well as in-situ and applied stresses. In our simulations, only gravitational stresses were considered, while no other natural in-situ stresses were assumed to have an influence on the slope behaviour. The boundary conditions chosen for the static model domain fix the velocity normal to the boundaries (lateral borders and bottom of the model). The static equilibrium state is measured with the maximum out-of-balance force, i.e. the net nodal force vector at each gridpoint of block, compared to the total applied forces. In a first stage, models were run to a static equilibrium (i.e. unbalanced force ratio $<10^{-5}$) under gravity loading (z = -9.81 m/s²); auto damping was applied and mass scaling was enabled.

A strength reduction analysis of block material and joint surfaces was performed for the geomechanical parameters that quantify plastic deformation. This analysis evaluates the sensitivity of the chosen values in terms of static slope

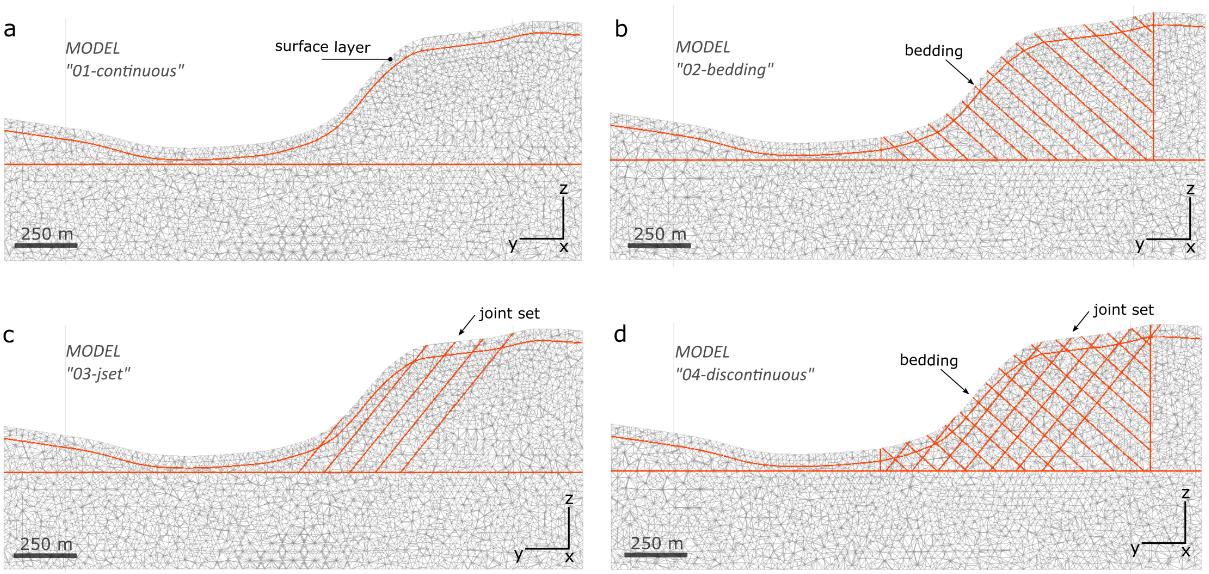

Figure 6: Cross section of the structural model configurations with continuous rock mass (*01-continuous*; a), with implemented flysch bedding planes only (*02-bedding*; b), with joint set only (*03-jset*; c), and setup with bedding planes and crossing joint set combined (*04-discontinuous*; d); cf. inset figure in Figure 4. Note, the near-surface layer pointed out in (a) was modelled in all configurations and represents the weaker material and joint strength at the slope surface (cf. Tab. 1 and 2).

stability with the factor of safety (FoS). The FoS solution implemented in the Itasca codes uses the strength reduction method that is commonly applied in slope stability analyses; it is based on the Mohr-Coulomb failure criterion and the Coulomb-slip model employing a progressive reduction of material or joint strength until failure occurs.

The strength reduction thereby concentrates on the parameters of cohesion C and friction angle ϕ (separately or combined) according to:

$$C^{trial} = \frac{1}{FoS^{trial}}\, C \tag{1}$$

and

$$\phi^{trial} = \arctan\left(\frac{1}{FoS^{trial}}\ \tan\phi\right) \tag{2}$$

where the superscript *trial* designates the trial values used during the strength reduction calculations.

The bracketing approach implemented in the software uses a similar technique to Dawson et al. (1999) that determines initial stable and unstable bracketing states for the system. These brackets are then progressively narrowed by reducing the space between stable and unstable solutions below a specified tolerance (default value of 0.005); as a result, a stable or unstable solution is found. The number of used solution cycles thereby varies according to the characteristic response time of the model (depending on the assigned material strength). Over one averaged current span of cycles, a mean value of force ratio is calculated and compared with the mean force ratio of the previous span of cycles; the cycling stops when the bracketing tolerance is reached, otherwise another loop is executed. The stable solution designates a system in equilibrium state, while an unstable solution indicates a system in continuing motion. In a static analysis, for a system at zero stress rate (i.e. no external stresses are applied), only gravity is considered as system load during FoS calculations.

For this analysis, we used the basis model structure (cf. Figure 6a) with uniform slope material in order to test the sensitivity of the selected model parameter; calculations were performed within a range of 25% of the peak and residual values, respectively.

3.2.3. Dynamic conditions

The dynamic modelling domain aims for a model solution under dynamic loads that generate and dissipate kinematic energy for a short duration and high frequency (e.g., seismic or explosive loads). Two different boundary conditions are used for the model bottom and lateral boundaries, i.e. viscous and free-field conditions, respectively. At the lateral model boundaries, we define boundary conditions that account for free-field motion without lateral constraints (infinite model). The latter, originally introduced by Cundall et al. (1980), allows upwards propagating energy to fully move as plane wave without being absorbed at the model boundaries. A non-reflecting viscous boundary is applied at the model base as it uses independent absorption points at the model borders, i.e. scattering of outgoing wave energy back inside the model is suppressed (Lysmer and Kuhlemeyer, 1969). For earthquake simulations, a common approach to overcome the non-reflecting boundary at the model bottom is the introduction of wave energy in form of a stress instead of velocity history according to:

$$\sigma_n = 2\,(\rho\, V_P)\, C_n \tag{3}$$

and

$$\sigma_S = 2\,(\rho\, V_S)\, C_S \tag{4}$$

where σ_n and σ_S are the applied normal and shear stress, ρ the mass density, and V_P and V_S the P-wave and S-wave propagation through the medium, respectively. C_n and C_S represent the input normal and shear velocity, respectively, and are given by:

$$C_p = \frac{K \ + \ 4G/3}{\rho} \tag{5}$$

and

$$C_s = \sqrt{G/\rho} \tag{6}$$

where K is the bulk modulus, G the shear modulus and ρ the dry density of the material.

In this regard, the finite-difference (FD) element size is defined following the law of Kuhlemeyer and Lysmer (1973) to guarantee accurate numeric wave transmission through the medium according to:

$$\Delta l \leq \frac{\lambda}{10} \quad to \quad \frac{\lambda}{8} \tag{7}$$

where Δl is the FD spatial element size and λ the wavelength associated with the highest frequency component of input wave. For the presented models, the latter relation allows a complete energy transmission in the frequency range of 1.8 to 5.5 Hz for the chosen FD element size of 30 m.

A common approach for synthetic reproduction of earthquake signals is the Ricker wavelet which is able to approximate the spectral content of recorded earthquake signals (cf., Gholamy and Kreinovich, 2014). The function was introduced by Ricker (1953) as follows:

$$A = (1 - 2\pi^2 f^2 t^2)\ e^{-\pi^2 f^2 t^2} \tag{8}$$

where A is the amplitude, f the central frequency and t the time.

In the frame of this work, a synthetic Ricker multiplier that combines a low- and a high-frequency part, notably with the central frequencies 1.4 and 3.5 Hz, was used to test the seismic loading of the Balta slope. The signal is applied at the model base as stress-time history during three excitation sequences (total duration of 14 seconds). The applied stress amplitude is 1 MPa in x- and y-directions, reproducing a shear stress in lateral directions and resulting in an input acceleration of 1 m/s^2, i.e. approximately 0.1g.

In addition, the effect of real ground acceleration data on the modelled Balta pre-failure slope was tested with an event record from the 2014 Iquique earthquake (Chile), which accounts for subduction zone mechanisms as observed in the Vrancea seismic zone (cf., Bokelmann and Rodler, 2014). The offshore M_W 8.2 earthquake of April 1, 2014, occurred 94 km NW of Iquique at the western coast of North Chile in 25 km depth. It can be described as megathrust event caused by the convergence the Nazca and South America plates (Piña-Valdés et al., 2018; USGS, 2020). The data used for our simulations was recorded 170.2 km distant from the epicenter (Chusmiza station, National Seismic Network of Chile); the input signal is shown in Figure 7 in terms of applied velocity and acceleration. The earthquake record was implemented at the model bottom as stress-time history in x- and y-direction (representing upwards propagating shear stresses) during 120 seconds.

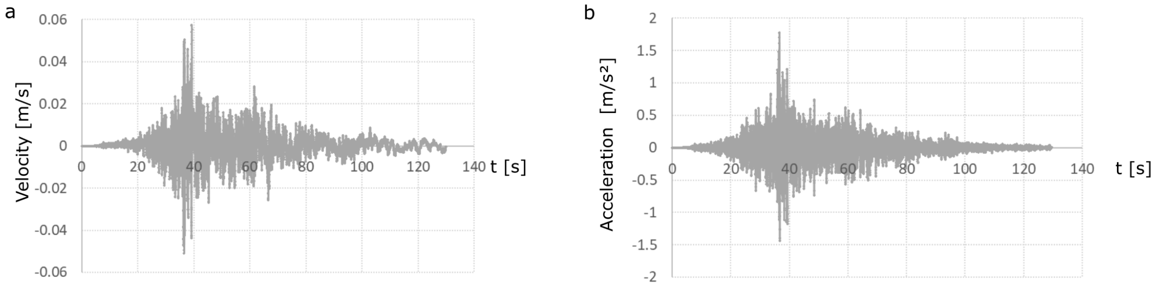

Figure 7: 2014 Iquique event (a) velocity and (b) acceleration record used for the dynamic loading of the reconstructed Balta slope.

The mechanical damping applied in a dynamic analysis should account for the energy loss in the natural system during dynamic loading, while for a natural ground (soils and rocks), damping can be considered as frequency-independent (cf., Cundall, 1976). Rayleigh damping offers a numerical solution to overcome this limitation and provides a approximately hysteretic solution over a defined frequency range (cf., Bathe et al., 1975; Biggs, 1964); here, a Rayleigh damping of 2% is applied (for geological materials a Rayleigh damping of 2-5% is recommended, cf., Biggs, 1964).

In order to quantify the site effects of the modelled Balta slope, we computed standard spectral ratios (SSR) of acceleration records between two points of the model domain with seismic Ricker loading. The numerical SSR's compare the signal response of the original input wave (here, at the model basis) with the signal response at a chosen observation point (here, at the model surface) in the frequency domain. Such analysis is applied in multiple numerical studies to quantify the site effects of landslide prone slopes, e.g., Havenith et al. (2002); Gischig et al. (2015); Luo et al. (2020). The SSR analysis was performed for two case scenarios, i.e. SSR01 that was constructed with intact bedrock material, and SSR02 that uses both, near-surface and intact bedrock material (cf. Tab. 1). For both SSR analyses, the dynamic input was modelled with a shear stress propagating from the model bottom upwards in y-direction (i.e. N-S, direction of the slope), in x-direction (i.e. E-W) and combined in x-y-direction. The acceleration record at the model base was used as artificial reference station (signal amplitudes multiplied by two); the reference signal is compared to the record at the slope surface and top (cf. Figure 5; history points 'slope' and 'top').

4. Results

4.1. Static strength reduction analysis

For all models, a static solution was obtained with the used input parameters; the slope is considered as initially stable and does not suggest failure in its in-situ conditions. The static model response was tested in terms of joint strength with elastic block material. As shown on the right column of Figure 8, the static model exclusively responds to changes of the joint's friction angle φ. While the overall slope is evaluated with a FoS of 2.23 with $\varphi = 42°$ (used for the intact bedrock material in our simulations), its stability decreases to a FoS of 1.32 with $\varphi = 28°$ (used for the surface material in our simulations). By decreasing φ to 21°, i.e. 28° reduced by 25%, the overall slope is classified as unstable (FoS = 0.95). For the variations in joint cohesion c (using a constant φ of 42°), the slope shows a FoS of 2.23 for all calculations, demonstrating that the joint strength is conditioned by the selected φ.

The sensitivity of material parameters was evaluated in terms of block internal cohesion C and internal friction angle ϕ. For these tests, the Mohr-Coulomb criterion and a constant joint friction angle φ of 30° were chosen. As shown in the right column of Figure 8, the FoS calculations of the material variations all show the constant result of 1.51 (with a negligible decrease to 1.49 for the minimum value of internal block cohesion). Again, the FoS result of 1.51 is controlled by the joint friction angle φ of 30° rather than by the varied material strength.

4.2. Ground acceleration and amplification analysis

Based on the initial stress state of the model, the slope model is analysed in terms of dynamic wave transmission that simulates ground acceleration. Here, the excitation with the Ricker input signal accounts for the elastic response of the slope; results are shown in Figure 9 for the two scenarios of the *01-continuous* model configuration (cf. Figure 6a), i.e. the uniform material model of bedrock and a layered model with a surface-near weaker material (that was observed in the field and is used herein for the failure simulations). The uniform model reaches a PGA of 0.35g and 0.2g in y- and x-direction, respectively, at the model surface (recorded at the history point 'top', cf. locations in Figure 5). The two-layered model produces PGA values of 0.5g and 0.4g in y- and x-direction, respectively; the implication of a surface-near layer with reduced material strength results thus in more pronounced acceleration values at the slope surface.

The numerical computation of standard spectral ratios between two reference points in the model (notably the model base vs slope surface 'slope' and crest 'top', cf. history point locations in Figure 5) is used to further analyse

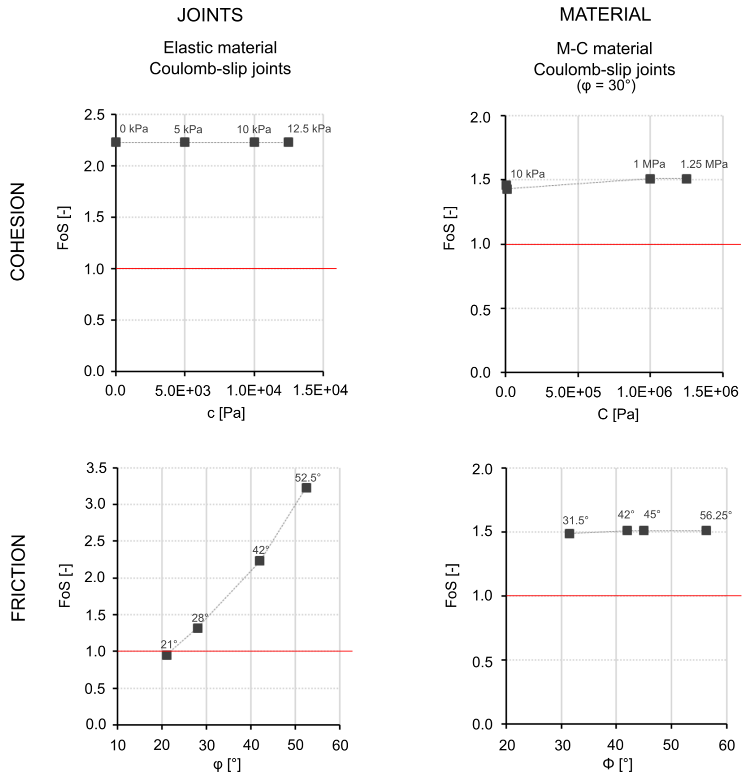

Figure 8: Strength reduction analysis of plastic parameters of joints (left column) and block material (right column).

the dynamic amplification potential of the reconstructed slope; results are presented in the frequency-domain (see Figure 10). SSR01 (Figure 10a; uniform bedrock material) shows relatively low amplitude frequency responses at the slope; however, at the top, we notice a pronounced amplification at 1 Hz of amplitude 5 for y-orientated (i.e. N-S) excitation, and a pronounced amplification at 2 Hz of amplitude 4 for the combined x-y-excitation. Similar to the uniform material model, SSR02 (Figure 10b; with surface-near weaker material) indicates no significant amplification at the slope receiver. For the top, pronounced amplifications of amplitude >4 appear at 0.8 Hz and 1.5 Hz for the y-excitation (N-S), at 1 Hz for the x-excitation (E-W) and at 2-2.5 Hz for the combined x-y-record.

For the top receiver, we notice a doubling in the amplification factor for the characteristic ∼2 Hz peak at x-y-orientated excitation between the SSR01 and SSR02 scenarios. This shows that, even if amplification of seismic waves is due to topographic effects at the slope crest, the weaker near-surface layer intensifies shaking effects. The same phenomenon can be noticed for the x-orientated excitation at the top. Note, the amplification results of both scenarios at the top receiver in the frequency range of 1.2-1.5 Hz and 2-2.5 Hz have been observed by actual measurements that we performed at the crest and analysed in terms of HVSR (presented in Mreyen et al., 2021) and confirms the numerically produced 1.2-2 Hz frequency peaks at the hill crest. The latter validates the model response in terms of seismic wave transmission at the original mountain crest.

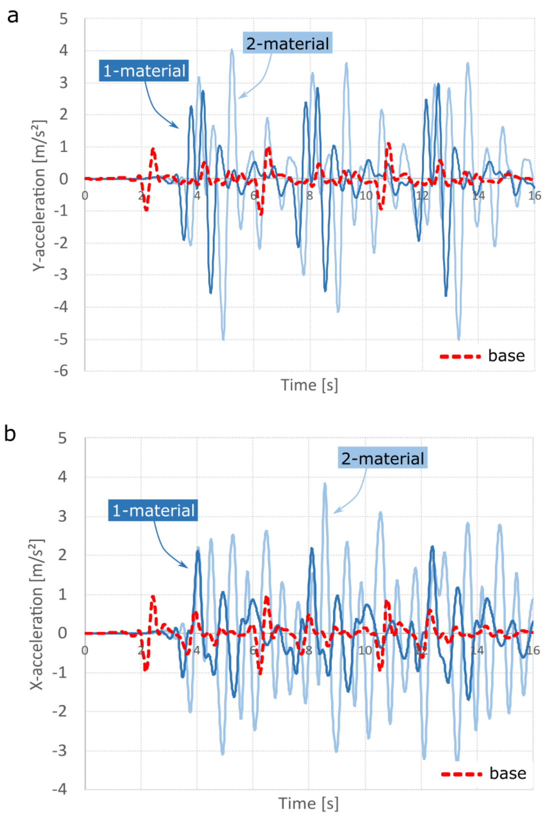

Figure 9: Elastic model response of the *01-continuous* model configuration (cf. Figure 6a) in terms of (a) y-acceleration and (b) x-acceleration at the model base (red curve) and model top (blue curves; cf. history point locations in Figure 5). The 1-material test refers to a uniform bedrock material model; the 2-material test adds the near-surface material with weaker properties in the upper 50 m (see Table 1.

4.3. Reproduction of slope failure

For the numerical simulation with seismic loading, we use the beforehand introduced Ricker excitation (cf. Eq. 8) as well as the earthquake record of the 2014 Iquique event (Chile; cf. Figure 7) simulating a thrust event of intermediate depth. In Figure 11, we show the model behaviour of the slope with implemented discontinuities after 14 s of ground acceleration (three successive Ricker wavelets in x- and y-direction, producing PGA values of 0.1 to 0.2 g at the model surface) with a changed displacement pattern for the two different structural configurations, i.e. with joint set only, model *03-jset*, and with bedding planes crossed by the joint set, model *04-discontinuous* (cf. Figure 6c and d, respectively). The *03-jset* model shows most pronounced values at the frontal part of the slope, while the *04-discontinuous* model triggers block motion in larger depth; the model reaction is thus highly influenced by the implementation of bedrock bedding planes.

In the following, the *04-discontinuous* model configuration was chosen for the slope failure simulations as it represents the most realistic conditions. Moreover, in order to overcome the numerical limitations of creating a natural

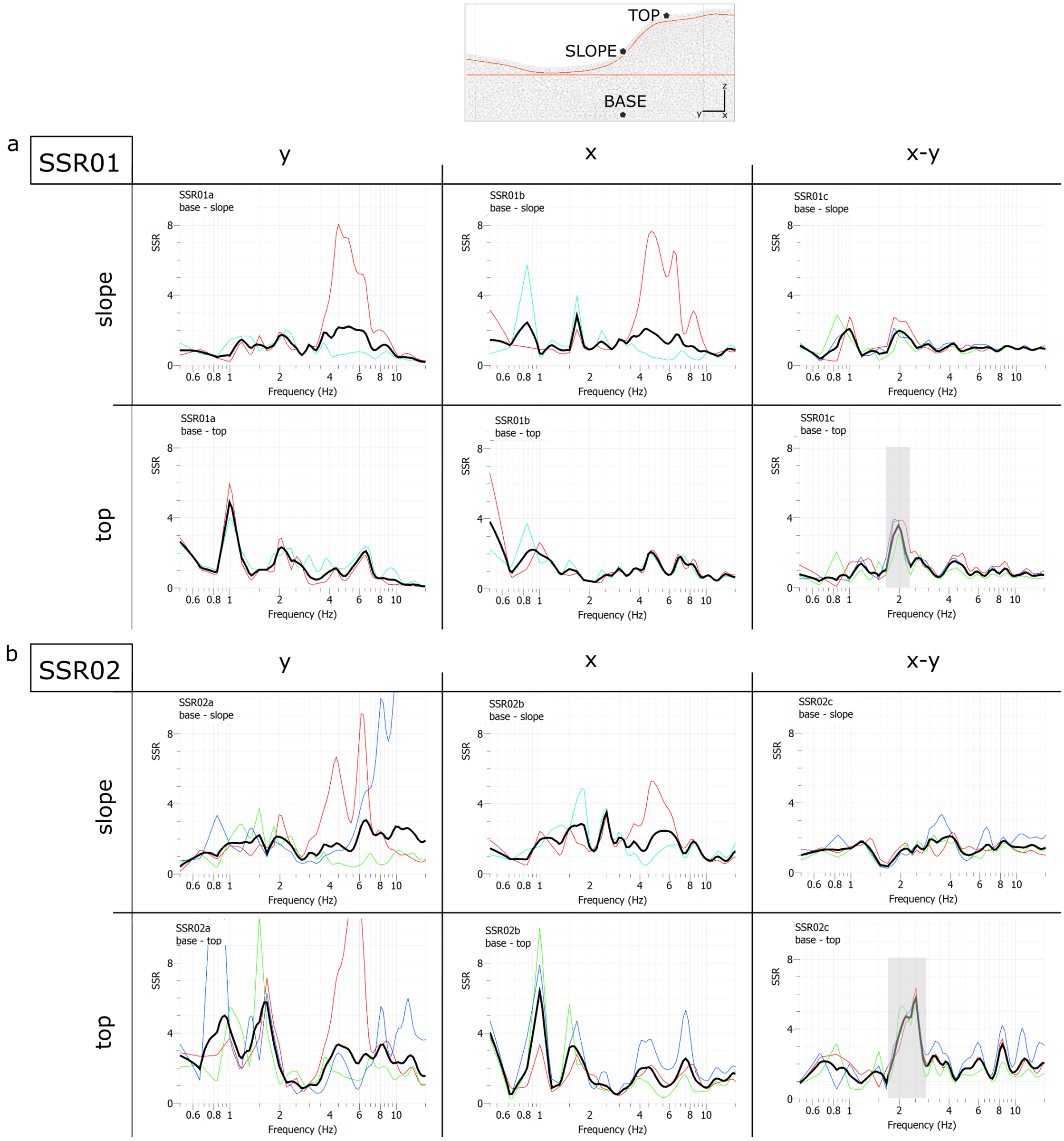

Figure 10: Site effect analysis in the elastic domain: (a) uniform material configuration SSR01 and (b) two-layered configuration with weaker surface material SSR02. The black line represents the averaged SSR response. The grey bars mark a characteristic frequency response of ~2Hz for all models at the top receiver.

rupture surface in a tetrahedral block environment and to facilitate initial detachment of rock mass, an auxiliary rupture surface was modelled in form of a fixed joint plane, i.e. allowing for strength reduction of joint material only after initial block motion occurred (using residual geomechanical parameters); a similar approach has been applied by Havenith et al. (2003a) and Gischig et al. (2016) in the 2D domain. This pre-determined rupture surface was implemented with a dip of 15° in slope direction, while the strength properties assigned to the plane account for a superior

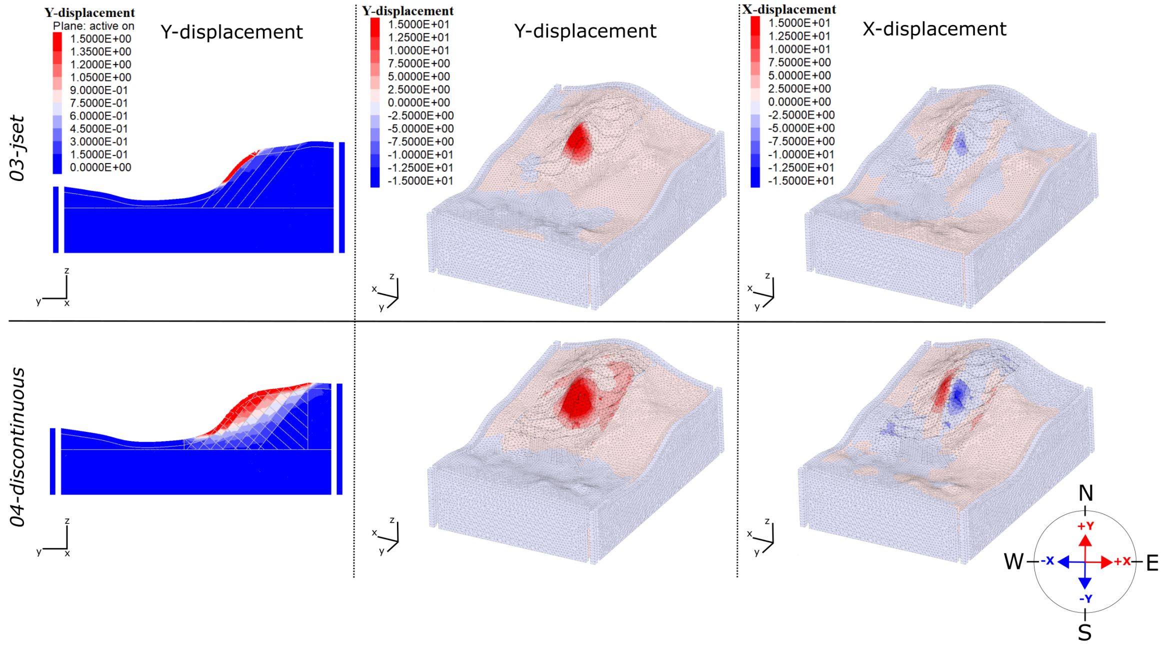

Figure 11: Y- and x-displacement of blocks after 14 seconds of dynamic loading with the Ricker multiplier for the jset model configuration (*03-jset*; cf. Figure 6c) and the jset-bedding model configuration (*04-discontinuous*; cf. Figure 6d).

joint friction angle, i.e. φ of 20°, and a residual φ of 17.5° that is only assigned after initiation of motion. A cross section of the model structure with integrated auxiliary sliding plane is given in Figure 12a. Figure 12b shows the displacement magnitude of block centroids after reaching static equilibrium; maximum displacements concentrate on the slope front (approximately 0.6 m), whereas no significant sliding occurs along the pre-determined rupture surface. The slope is thus considered as statically stable.

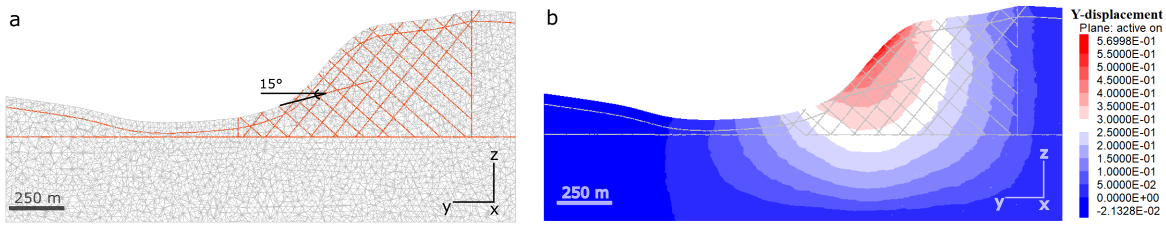

Figure 12: Cross section of the *04-discontinuous* model: (a) model structure with integrated 15° dip ($\varphi = 20°$) auxiliary rupture surface; (b) y-displacement contours in static equilibrium state.

4.3.1. Ricker excitation

The triple Ricker wavelet excitation was introduced at the model base in x- and y-direction. The total duration of cycling was set to 60 seconds of which the first 14 seconds account for the dynamic input duration (i.e. simulated time, calculated by the time step of one numerical cycle); block displacement, velocity and acceleration are recorded at the defined history points. The critical time of first block detachment is monitored by the shear displacement along the rupture surface using two history points: a first history point is located at 15 m (i.e. in the near-surface layer), and a second at 250 m from the model surface along the auxiliary joint plane. For the shear displacement along the sliding horizon, a first block detachment is recorded after 1.2 seconds (shear displacement of 0.15 m) at the surface near history point, and after 9.3 seconds (shear displacement of 9.92 m) at the second point; i.e. in comparison to the intact bedrock, failure of the weaker near-surface layer initiates after a relatively short period of seismic vibrations.

In Figure 13, y-displacement of blocks is shown along a cross section at different stages. After the synthetic Ricker loading (first 14 simulated seconds), the layer limited by the first joint plane is completely detached and forms an initial scarp of approximately 15 m height (Figure 13e). The initial failure can be characterized as shear dominated, while tension driven failure of blocks is only secondary. With further cycling, the blocks stay in motion due to the residual velocity of blocks. After the triggering of the first block layer, we notice the dragging of the second block layer due to the mass movement and the collateral stability reduction at the top and foot of the layer. After 60 seconds of cycling (i.e. simulated time), an initial detachment scarp height of approximately 150 m is produced (Figure 13i), approaching the actual scarp height of 250 m of the Balta rockslide. Maximum displacement occurred at the history point 'CP', which is the point of highest curvature at the slope surface (cf. location in Figure 5), with a total displacement magnitude of 423.03 m (of which 327.18 m account for y-displacement, i.e. in slope direction, 109.28 m for x-displacement, i.e. E-W, and 244.87 m for negative z-displacement, i.e. downwards). The highest velocity magnitude was reached at 'CP', while maximum acceleration were measured at the history point 'E-Surf' that monitors kinematic behaviour at the eastern slope surface.

4.3.2. Earthquake simulation

The Iquique earthquake record (cf. Figure 7) was introduced at the model basis in x- and y-direction with a duration of 120 seconds and model computations were maintained during additional 110 seconds. Figure 14 shows the result of block motion along a central cross section during different cycling periods (note, seconds relate to the simulated time). A first detachment scarp is visible after approximately 10 seconds of induced seismicity and a superficial layer of rock collapses during the first 60 seconds of ground acceleration. In the course of this collapse, the material bulges up at the central part of the slope, before running down to the valley. The failure of underlying block layers initiate at the foot of the modelled sliding plane, while motion also accentuates at the upper front of the slope. We also notice expulsion of smaller blocks along the sliding plane and fracturing of the material during their down slope displacement. Recorded maximum displacements accentuate at the 'CP' history point (see location in Figure 5) with a three-component magnitude of 925.9 m (absolute values of 94.9 m, 857.2 m and 344.2 m in x-, y-, and z-direction, respectively). Maximum x-displacement was recorded at the eastern slope flank with 342.21 m at the history point of

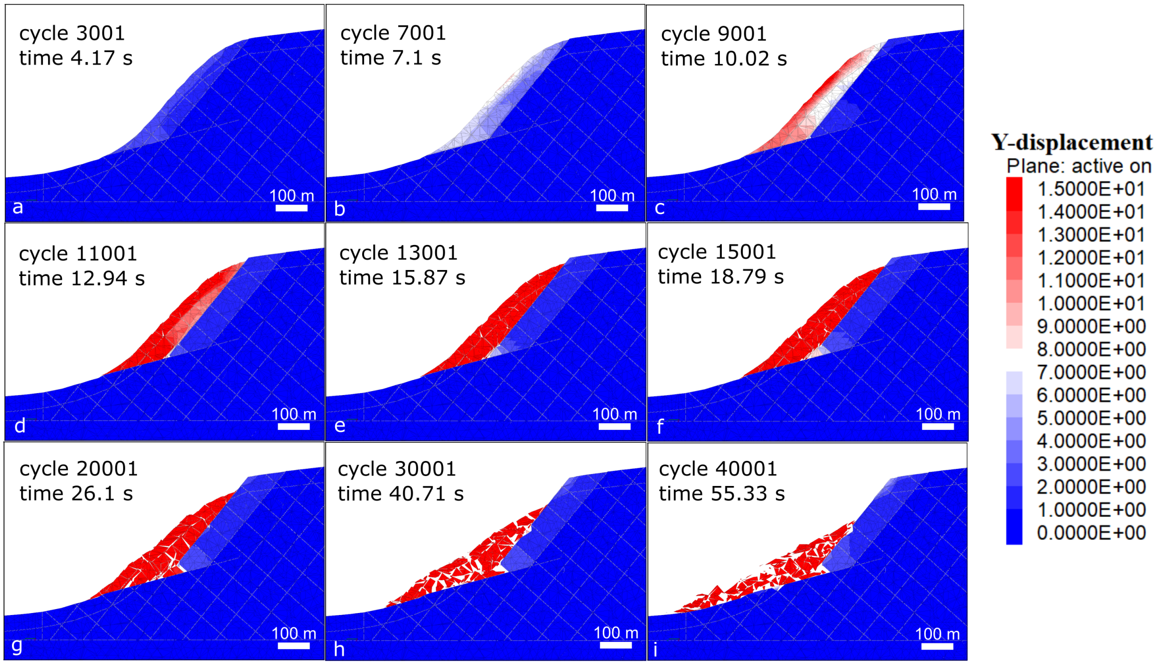

Figure 13: Cross section showing Y-displacement contours of blocks during dynamic loading with Ricker wavelet; duration of dynamic load is 14 simulated seconds, i.e. landslide triggering (a-d), and residual block motion after seismic shaking (e-i).

334 the eastern slope flank 'E-surf' as well as highest peak acceleration. Highest velocity occurred at the history point of
335 the western slope flank 'W-Surf', i.e. the surface point of the western slope flank.

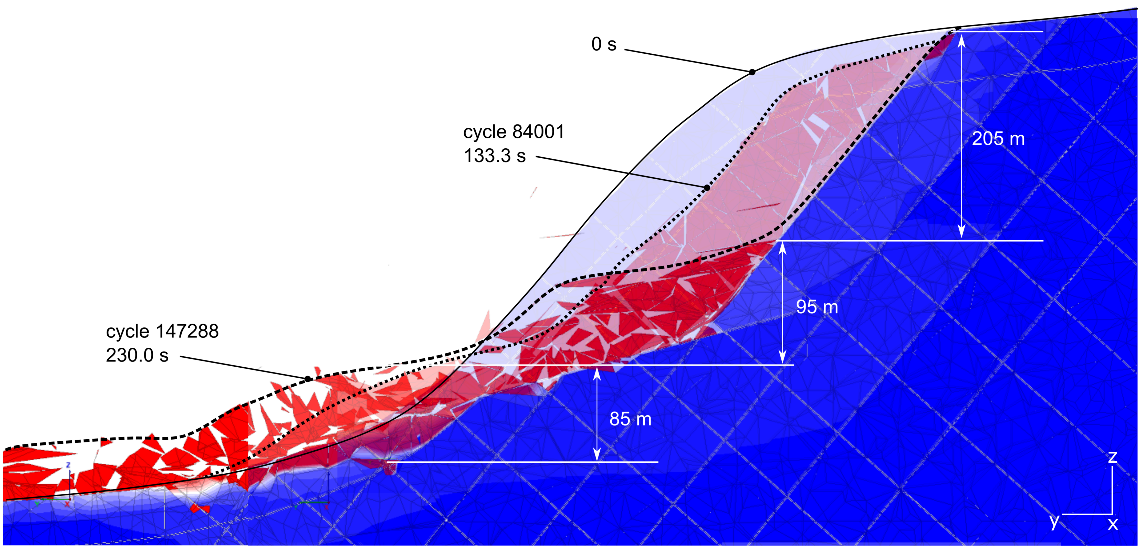

Figure 14: Simulation of the Balta failure after 0, 133.3 and 230 simulated seconds (of which the first 120 s account for dynamic loading with the 2014 Iquique signal) shown on a central cross section.

A large mass of debris reached the valley after a total cycling duration of 120 seconds. Furthermore we observe a pronounced lateral spread of material; the eastern slope flank tends to collapse in a purely eastwards motion, before the debris runs out towards the valley to the NE, while the western slope seems to be predominated by a NW-orientated motion.

Subsequent mass entrainment was observed during the additional seconds after ground acceleration as a result from residual block velocity; especially the inner slope and slope top (history points 'slope mid' and 'top') are subject to these entrainments with an increased velocity magnitudes during 60-80 seconds after the initial ground acceleration. In Figure 14 the slope morphology is shown along a central cross section for three different stages of cycling; the morphology is marked by the additional downhill orientated motion of blocks as well as the material bulging below the scarp and at the middle part of the slope; here, we also observe the fracturing of the material at the landslide basis, i.e. the former slope surface, resulting in a larger thickness of collapsed material in addition to the source zone's debris. The final modelled landslide thickness reaches values of 85-95 m. The scarp formation follows the inclination of the modelled joint planes and reaches a height of approximately 200 m after 230 s of cycling, approaching its actual height of 250 m. Figure 15 shows the final model result after the simulated time of 230 s (of which the first 120 s account for the seismic loading with the Iquiuque signal).

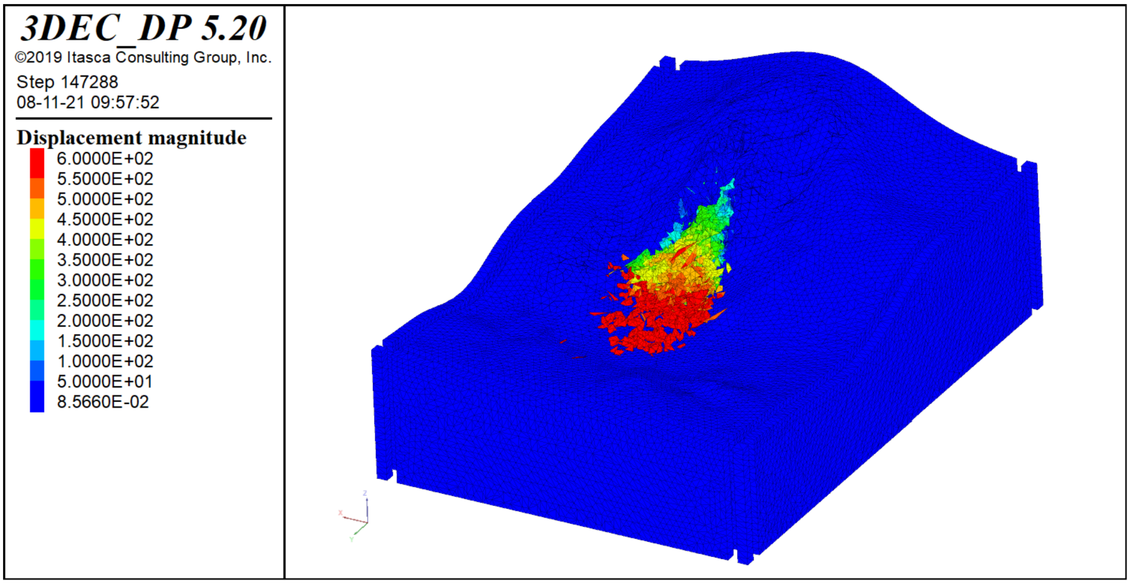

Figure 15: Balta failure after 230 simulated seconds, shown in terms of block displacement magnitude [m].

5. Discussion

For the slope reconstruction of Balta, we used a three-dimensional volume balancing approach that proved efficient, nevertheless also presents uncertainties, i.e. other than the determined landslide volume, we have no quantifiable control over the original morphology prior to landsliding. We can only estimate, on the one hand, the material loss as a consequence to slope and river erosion, and on the other hand, the volume expansion as a cause of material detachment (expressed in terms of bulking factor). The presented solution is one out of multiple possible scenarios; nevertheless, the chosen pre-failure model is considered to be representative, since it allows to understand the relation of in-situ geomechanical properties and structural settings that were derived from field measurements. Furthermore, it is based on a realistic morphology reproducing neighbouring slope shapes that are not affected by landsliding. In addition, seismic wave transmission and amplification tests could show the validity of the model domain by numerically reproducing seismic site effects similar to those measured at the in-situ rock above the source zone of the landslide.

The geomechanical approach to simulate failure development of the Balta slope (including simulated internal fracturing of rock mass) is principally based on measurements and field observations, i.e. the structural setting of the flysch bedrock, the fracture degree of landslide debris, the elasto-plastic properties as well as the fair to poor rock quality of in-situ rock. Even though we allow for internal fracturing of rock, in the dynamic domain, we observe a failure development that is predominated along the discontinuities cutting through the rock mass and the modelled sliding surface. This can be due to the tetrahedral form of the model elements constituting the rock mass; once the rock mass is mobilised, an internal fracturing of rock mass can be noted. However, observations on co-seismic rockslides in Central Asia by Strom (2010) could show a similar sequential deposition mechanism of landslide mass, supposedly guided by discontinuities such as joints or rock stratigraphy. The impact of modelled joint dip angle and orientation is further outlined by the parametrical studies of the Balta slope in the 2D domain presented in Lemaire et al. (2020), where it is shown that the displacement pattern of seismically induced motion strongly depends on the defined structures. The actual case of Balta, as implemented in this work (with 55° anti-dip slope bedding and counter cutting joint planes), is marked by a lenticular displacement contour indicating rotational sliding. A failure shape even closer to the actual state could possibly be produced by implementing more closely spaced joint planes, while this solution would significantly increase the related computational effort and was not feasible in the frame of this work.

For the Iquique earthquake simulation, the general block motion is directed towards the valley; however, the x-component of block displacements demonstrates a 3D effect probably due to the morphology of the modelled pre-failure slope topography and the combined x-y-orientated stress induced at the model bottom. This effect causes lateral expansion of landslide debris to a broader extent than the source zone width at the relatively narrow head scarp - a result that is in accordance with the actual post-failure debris distribution apparent in our study area. Subsequently to the period of ground acceleration, the run-out kinematics of the material are driven by the residual block velocity leading to mass entrainment during an extended period of time.

In terms of travel distance, the debris mass reaches the valley bottom after the modelled 230 seconds; considering the rapid and voluminous failure, the Balta rockslide could possibly have caused the blockage of the river. As mentioned in Mreyen et al. (2021), the opposite slope of Balta was also subject to former landsliding, which in case of simultaneous triggering, could even have led to the formation of a temporary barrier lake in the valley. As the computed slope behaviour shows a layered detachment of rock along the modelled joint planes, it can be concluded that the debris reaching the valley originates from the upper surface-near slope layers, and is supposedly marked by a high fracture degree due to the long travel distance (>500 m) from depletion to accumulation zone. Rock layers located in more profound depths only initiate significant motion after the collapse of the former. The source zone of the rock mass forming the *plateau* area is thus supposedly located in the inner slope as demonstrated by the models; according to our geophysical prospections (cf., Mreyen et al., 2021), the rock mass might consequently be less fractured due to the relatively higher rock strength at the inner slope, as well as the limited travel distance to the depositional area (supposedly caused by the increasing friction of rockslide debris along the rupture surface and related kinetic energy loss).

The numerical modelling results provide valuable insights in the kinematics and possible processes implicated in the landslide development. While the morphological shape of the actual Balta slope could be simulated close to the observed one, it could not be entirely reproduced (especially in terms of scarp height and depth). As mentioned above, more detailed structural modelling, e.g. closer and more numerous joint planes, could possibly increase post-failure accuracy. Another key element to be discussed in this regard is the possible effect of soil moisture and groundwater in the pre-failure slope, that supposedly could have an important impact on dynamic modelling results due to elevated water pressures. This latter aspect was not considered due to the computational complexity of the 3D dynamic domain, but also the uncertainty related to the local pre-historic groundwater regime given the advanced age of the landslide. Indeed, the region of the Flysch Carpathians is marked by a rather humid continental climate and the aspect of groundwater fluctuations, supposedly reducing slope stability of the area significantly, should not be neglected. Still, we suggest that extensive rainfall periods and elevated water saturation cannot be considered as unique trigger factors for the deep-seated Balta slope failure, as these climatic phenomena typically cause rather superficial slides and flows in the region. Based the numerical analyses presented in this work, we consider one or multiple seismic events, possibly combined with climatic factors (long- to short-term), to be at the origin of the Balta slope failure.

6. Conclusions

The pre-historic Balta rockslide in the seismically active part of the Romanian Carpathian Mountains was back-modelled to pre-failure conditions in terms of topographical, structural and geomechanical settings and introduced to a 3D distinct element environment. Static analyses could show that the estimated pre-failure slope acts as stable under gravitational loading. Seismic shaking was modelled with a synthetic Ricker wavelet and a real earthquake record of a subduction event; the introduced signals are characterized by PGA values of 0.1-0.2 g at the model surface in x- and y-directions, and produce frequency peaks of 1.2-2.5 Hz at the hill crest (a frequency range that was also measured by actual seismic tests above the slope crown). The reproduction of slope failure could be simulated with the implementation of rupture surface at the landslide basis and several seconds of seismic shaking. The sliding motion is thereby predominately guided by the implemented joint planes, while internal failure of rock mass initiates in form of brittle fracturing after the triggering of block motion by seismic shaking. During this back-analysis, specific morphological markers, such as the landslide scarp and central *plateau* area, could be reproduced; the material reaches the valley with maximum displacements of approximately 1350 m and marked by a lateral, slightly E-accentuated, expansion. Provided that the chosen pre-failure model approximates real conditions, our analyses show a probable co-seismic development of the Balta slope; the latter might be extended to other pre-historic slope instabilities in the valleys of Vrancea-Buzau and the Carpathian mountains. Such an extended analysis would constitute valuable new information for future seismic hazard estimations of the region.

7. Acknowledgements

This research was partly funded by the WBI (with a bilateral project ′*Evaluation des risques long-termes liés aux mouvements de masse déclenchés par les séismes dans la région de Vrancea, Roumanie*′), as well as by the F.R.S-FNRS Belgium in the frame of the FNRS-SNF collaboration project ′4D seismic response and slope failure′. We further acknowledge the FRIA-FNRS research fellowship granted to Anne-Sophie Mreyen during the years 2016-2020.

References

Baron, I., Agliardi, F., Ambrosi, C., and Crosta, G. B. (2005). Numerical analysis of deep-seated mass movements in the Magura Nappe; Flysch Belt of the Western Carpathians (Czech Republic). *Natural Hazards and Earth System Sciences*, 5(3):367–374.

Bathe, K.-J., Ramm, E., and Wilson, E. L. (1975). Finite element formulations for large deformation dynamic analysis. *Int. journal for numerical methods in engineering*, 9(2):353–386.

Berti, M., Bertello, L., Bernardi, A. R., and Caputo, G. (2017). Back analysis of a large landslide in a flysch rock mass. *Landslides*, 14(6):2041–2058.

Biggs, J. (1964). *Introduction to structural dynamics*. McGraw-Hill College.

Bokelmann, G. and Rodler, F.-A. (2014). Nature of the Vrancea seismic zone (Eastern Carpathians)–New constraints from dispersion of first-arriving P-waves. *Earth and Planetary Science Letters*, 390:59–68.

Bonilla-Sierra, V., Scholtes, L., Donzé, F., and Elmouttie, M. (2015). Rock slope stability analysis using photogrammetric data and dfn–dem modelling. *Acta Geotechnica*, 10(4):497–511.

Bourdeau, C. and Havenith, H.-B. (2008). Site effects modelling applied to the slope affected by the suusamyr earthquake (kyrgyzstan, 1992). *Engineering Geology*, 97(3-4):126–145.

Bozzano, F., Lenti, L., Martino, S., Montagna, A., and Paciello, A. (2011). Earthquake triggering of landslides in highly jointed rock masses: Reconstruction of the 1783 scilla rock avalanche (italy). *Geomorphology*, 129(3-4):294–308.

Bozzano, F., Lenti, L., Martino, S., Paciello, A., and Scarascia Mugnozza, G. (2008). Self-excitation process due to local seismic amplification responsible for the reactivation of the salcito landslide (italy) on 31 october 2002. *Journal of Geophysical Research: Solid Earth*, 113(B10).

Burjánek, J., Gischig, V., Moore, J. R., and Fäh, D. (2018). Ambient vibration characterization and monitoring of a rock slope close to collapse. *Geophysical Journal International*, 212(1):297–310.

Che, A., Yang, H., Wang, B., and Ge, X. (2016). Wave propagations through jointed rock masses and their effects on the stability of slopes. *Engineering Geology*, 201:45–56.

Crozier, M. (1992). Determination of palaeoseismicity from landslides. In *International symposium on landslides*, pages 1173–1180.

Cundall, P. (1976). Explicit finite differnce method in geomechanics. In *Second Int. Conf. Numerical Methods in Geomechanics, Blacksburg, 1976*, volume 1, pages 132–150.

Cundall, P., Hansteen, H., Lacasse, S., and Selnes, P. (1980). NESSI, soil structure interaction program for dynamic and static problems. *Norwegian Geotechnical Inst., Report*, pages 51508–9.

Dawson, E., Roth, W., and Drescher, A. (1999). Slope stability analysis by strength reduction. *Geotechnique*, 49(6):835–840.

Donati, D., Stead, D., Elmo, D., Karimi Sharif, L., Gao, F., Borgatti, L., and Spreafico, M. (2018). Experience gained in modelling brittle fracture in rock. In *52nd US Rock Mechanics/Geomechanics Symposium*. OnePetro.

Gholamy, A. and Kreinovich, V. (2014). Why Ricker wavelets are successful in processing seismic data: Towards a theoretical explanation. In *2014 IEEE Symposium on Computational Intelligence for Engineering Solutions (CIES)*, pages 11–16. IEEE.

Gischig, V., Eberhardt, E., Moore, J., and Hungr, O. (2015). On the seismic response of deep-seated rock slope instabilities — insights from numerical modeling. *Engineering Geology*, 193:1–18.

Gischig, V., Preisig, G., and Eberhardt, E. (2016). Numerical investigation of seismically induced rock mass fatigue as a mechanism contributing to the progressive failure of deep-seated landslides. *Rock Mechanics and Rock Engineering*, 49(6):2457–2478.

Havenith, H.-B., Jongmans, D., Faccioli, E., Abdrakhmatov, K., and Bard, P.-Y. (2002). Site effect analysis around the seismically induced Ananevo rockslide, Kyrgyzstan. *Bulletin of the Seismological Society of America*, 92(8):3190–3209.

Havenith, H.-B., Strom, A., Calvetti, F., and Jongmans, D. (2003a). Seismic triggering of landslides. Part B: Simulation of dynamic failure processes. *Natural Hazards ans Earth System Sciences*, pages 663–682.

Havenith, H.-B., Vanini, M., Jongmans, D., and Faccioli, E. (2003b). Initiation of earthquake-induced slope failure: influence of topographical and other site specific amplification effects. *Journal of seismology*, 7(3):397–412.

He, J., Qi, S., Wang, Y., and Saroglou, C. (2020). Seismic response of the lengzhuguan slope caused by topographic and geological effects. *Engineering Geology*, 265:105431.

Huang, R., Pei, X., Fan, X., Zhang, W., Li, S., and Li, B. (2012). The characteristics and failure mechanism of the largest landslide triggered by the wenchuan earthquake, may 12, 2008, china. *Landslides*, 9(1):131.

Hungr, O. and Evans, S. (2004). Entrainment of debris in rock avalanches: an analysis of a long run-out mechanism. *Geological Society of America Bulletin*, 116(9-10):1240–1252.

Hungr, O., Leroueil, S., and Picarelli, L. (2014). The Varnes classification of landslide types, an update. *Landslides*, 11(2):167–194.

Itasca (2016). *3DEC — Three-Dimensional Distinct Element Code (Version 5.2)*.

Itasca (2019). *Griddle (Version 1.0)*.

Iverson, R. M., Reid, M. E., and LaHusen, R. G. (1997). Debris-flow mobilization from landslides. *Annual Review of Earth and Planetary Sciences*, 25(1):85–138.

Jaboyedoff, M., Chigira, M., Arai, N., Derron, M.-H., Rudaz, B., and Tsou, C.-Y. (2019). Testing a failure surface prediction and deposit reconstruction method for a landslide cluster that occurred during Typhoon Talas (Japan). *Earth Surface Dynamics*, 7(2):439–458.

Jibson, R. W. (1996). Use of landslides for paleoseismic analysis. *Engineering geology*, 43(4):291–323.

Keefer, D. K. (1984). Landslides caused by earthquakes. *Geological Society of America Bulletin*, 95(4):406–421.

Khazai, B. and Sitar, N. (2004). Evaluation of factors controlling earthquake-induced landslides caused by Chi-Chi earthquake and comparison with the Northridge and Loma Prieta events. *Engineering geology*, 71(1-2):79–95.

Kim, D. H., Gratchev, I., and Balasubramaniam, A. (2015). Back analysis of a natural jointed rock slope based on the photogrammetry method. *Landslides*, 12(1):147–154.

Kogut, J. P., Pilecka, E., and Szwarkowski, D. (2018). Analysis of landslide effects along a road located in the Carpathian flysch. *Open Geosciences*, 10(1):517–531.

Krawiec, K. and Harba, P. (2019). Comparison analysis of numerically calculated slip surfaces with measured s-wave velocity field for Just-Tęgoborze landslide in Carpathian flysch. In *E3S Web of Conferences*, volume 133, page 01003. EDP Sciences.

Kuhlemeyer, R. L. and Lysmer, J. (1973). Finite element method accuracy for wave propagation problems. *Journal of Soil Mechanics & Foundations Div*, 99(Tech Rpt).

Lemaire, E., Mreyen, A.-S., Dufresne, A., and Havenith, H.-B. (2020). Analysis of the influence of structural geology on the massive seismic slope failure potential supported by numerical modelling. *Geosciences*, 10(8):323.

Li, L.-q., Ju, N.-p., Zhang, S., Deng, X.-x., and Sheng, D. (2019). Seismic wave propagation characteristic and its effects on the failure of steep jointed anti-dip rock slope. *Landslides*, 16(1):105–123.

Luo, J., Pei, X., Evans, S. G., and Huang, R. (2019). Mechanics of the earthquake-induced hongshiyan landslide in the 2014 mw 6.2 ludian earthquake, yunnan, china. *Engineering Geology*, 251:197–213.

Luo, Y., Fan, X., Huang, R., Wang, Y., Yunus, A. P., and Havenith, H.-B. (2020). Topographic and near-surface stratigraphic amplification of the seismic response of a mountain slope revealed by field monitoring and numerical simulations. *Engineering Geology*, 271:105607.

Lysmer, J. and Kuhlemeyer, R. L. (1969). Finite dynamic model for infinite media. *Journal of the Engineering Mechanics Division*, 95(4):859–878.

Marinos, P. and Hoek, E. (2001). Estimating the geotechnical properties of heterogeneous rock masses such as flysch. *Bulletin of Eng. Geol. and the Env.*, 60(2):85–92.

Marinos, P., Hoek, E., et al. (2000). Gsi: a geologically friendly tool for rock mass strength estimation. In *ISRM international symposium*. International Society for Rock Mechanics and Rock Engineering.

Maufroy, E., Cruz-Atienza, V. M., Cotton, F., and Gaffet, S. (2015). Frequency-scaled curvature as a proxy for topographic site-effect amplification and ground-motion variability. *Bulletin of the seismological society of America*, 105(1):354–367.

McNeel, R. et al. (2010). Rhinoceros 3d, version 5.0. *Robert McNeel & Associates, Seattle, WA*.

Meunier, P., Hovius, N., and Haines, J. A. (2008). Topographic site effects and the location of earthquake induced landslides. *Earth and Planetary Science Letters*, 275(3-4):221–232.

Moore, J. R., Gischig, V., Burjanek, J., Loew, S., and Fäh, D. (2011). Site effects in unstable rock slopes: dynamic behavior of the randa instability (switzerland). *Bulletin of the Seismological Society of America*, 101(6):3110–3116.

Mreyen, A.-S., Cauchie, L., Micu, M., Onaca, A., and Havenith, H.-B. (2021). Multiple geophysical investigations to characterize massive slope failure deposits: application to the Balta rockslide, Carpathians. *Geophysical Journal International*, 225(2):1032–1047.

Pal, S., Kaynia, A. M., Bhasin, R. K., and Paul, D. (2012). Earthquake stability analysis of rock slopes: a case study. *Rock Mechanics and Rock*

Engineering, 45(2):205–215.

Piña-Valdés, J., Socquet, A., Cotton, F., and Specht, S. (2018). Spatiotemporal variations of ground motion in northern Chile before and after the 2014 Mw 8.1 Iquique megathrust event. *Bulletin of the Seismological Society of America*, 108(2):801–814.

Ricker, N. (1953). The form and laws of propagation of seismic wavelets. *Geophysics*, 18(1):10–40.

Rocscience (2002). *RocLab (Version 1.0) - Rock Mass Strength Analysis using the Generalized Hoek-Brown failure criterion.*

Romeo, R. (2000). Seismically induced landslide displacements: a predictive model. *Engineering Geology*, 58(3-4):337–351.

Sassa, K. (1996). Prediction of earthquake induced landslides. In *Landslides*, pages 115–132.

Scholtès, L. and Donzé, F. V. (2015). A dem analysis of step-path failure in jointed rock slopes. *Comptes Rendus Mécanique*, 343(2):155–165.

Seequent (2021). *Leapfrog Geo*.

Sepúlveda, S. A., Murphy, W., Jibson, R. W., and Petley, D. N. (2005). Seismically induced rock slope failures resulting from topographic amplification of strong ground motions: The case of pacoima canyon, california. *Engineering geology*, 80(3-4):336–348.

Singeisen, C., Ivy-Ochs, S., Wolter, A., Steinemann, O., Akçar, N., Yesilyurt, S., and Vockenhuber, C. (2020). The Kandersteg rock avalanche (Switzerland): integrated analysis of a late Holocene catastrophic event. *Landslides*, pages 1–21.

Song, D., Chen, Z., Chao, H., Ke, Y., and Nie, W. (2020). Numerical study on seismic response of a rock slope with discontinuities based on the time-frequency joint analysis method. *Soil Dynamics and Earthquake Engineering*, 133:106112.

Stead, D. and Wolter, A. (2015). A critical review of rock slope failure mechanisms: the importance of structural geology. *Journal of Structural Geology*, 74:1–23.

Strom, A. (2010). Landslide dams in central asia region. *Journal of the Japan Landslide Society*, 47(6):309–324.

USGS, U. G. S. (2020). Earthquake Hazards - Event Page.

Wang, G. and Sassa, K. (2003). Pore-pressure generation and movement of rainfall-induced landslides: effects of grain size and fine-particle content. *Engineering geology*, 69(1-2):109–125.

Wang, G. and Sassa, K. (2009). Seismic loading impacts on excess pore-water pressure maintain landslide triggered flowslides. *Earth Surface Processes and Landforms*, 34(2):232–241.

Willenberg, H., Loew, S., Eberhardt, E., Evans, K. F., Spillmann, T., Heincke, B., Maurer, H., and Green, A. G. (2008). Internal structure and deformation of an unstable crystalline rock mass above randa (switzerland): Part i—internal structure from integrated geological and geophysical investigations. *Engineering Geology*, 101(1-2):1–14.

Zangerl, C., Chwatal, W., and Kirschner, H. (2015). Formation processes, geomechanical characterisation and buttressing effects at the toe of deep-seated rock slides in foliated metamorphic rock. *Geomorphology*, 243:51–64.

Zhu, Y., Dai, F., Yao, X., Tu, X., and Shi, X. (2019). Field investigation and numerical simulation of the seismic triggering mechanism of the Tahman landslide in eastern Pamir, Northwest China. *Bulletin of Engineering Geology and the Environment*, 78(8):5795–5809.